COMMUNICATION

Check for updates

Promising ITO-free perovskite solar cells with WO₃–Ag–SnO₂ as transparent conductive oxide†

Fengxia Liang,‡[a] Yi Lin,‡[ab] Zhenfei He,[c] Wei Chen,[b] Yudong Zhu,[b] Tian Chen,[b] Lin Liang,[a] Suman Ma, [ID][c] Yinghui Wu,[b] Bao Tu,[b] Dong Wang,[b] Zhixiang Zhang,[d] Linbao Luo [ID] *[d] and Zhubing He [ID] *[b]

Among various kinds of materials to substitute indium-tin-oxide (ITO) in rigid or flexible solar cells, oxide–metal–oxide (OMO) is one of the most promising. In this work, by means of reactive plasma deposition, a new combination of OMO structures, WO₃/Ag/SnO₂ (WAS), was deposited in one pot and each film thickness optimized to obtain high transmittance from 400 nm to 850 nm in wavelength and low sheet resistance, as well as mechanical robustness. The typical perovskite solar cells (PSCs) based on bare WAS composite film show poor device performance. Hence, aqueous soluble SnO₂ nanoparticles were applied to modulate the band level mismatch at the interface between the WAS and MAPbI₃ layers and the best-performing device with 14% conversion efficiency was achieved, which is the highest value reported hitherto with OMO structures as transparent conductive electrodes in PSCs. The results from various characterizations verify the interface engineering effect of the SnO₂ nanoparticles. The unencapsulated WAS-based device stability also is comparable to that of the ITO-based device in continuous light exposure in ambient atmosphere (37% RH and 60 °C). This work reveals a great potential of OMO in place of ITO in solar cells while it still needs more attention and efforts in continuing development.

Introduction

Owing to comparable transmittance and superior sheet conductivity, oxide–metal–oxide (OMO) materials have been

[a]School of Materials Science and Engineering, Anhui Provincial Key Laboratory of Advanced Functional Materials and Devices, Hefei University of Technology, Hefei, Anhui, 230009, China

[b]Department of Materials Science and Engineering, Shenzhen Key Laboratory of Full Spectral Solar Electricity Generation (FSSEG), Southern University of Science and Technology, No. 1088, Xueyuan Rd., Shenzhen, 518055, Guangdong, China. E-mail: hezb@sustc.edu.cn

[c]Department of Electrical and Electronic Engineering, Southern University of Science and Technology, No. 1088, Xueyuan Rd., Shenzhen, 518055, Guangdong, China

[d]School of Electronic Science and Applied Physics, Hefei University of Technology, Hefei, Anhui, 230009, China. E-mail: luolb@hfut.edu.cn

† Electronic supplementary information (ESI) available. See DOI: 10.1039/c8ta08287a

‡ Both authors contributed equally to this paper.

deemed as promising candidates to replace indium-tin-oxide (ITO) extensively used as transparent conductive oxide (TCO) both in the academic research community and in the related industries of optoelectronics devices. In contrast to other emerging candidates, such as silver nanowires, silver film, carbon nanotubes, graphene *etc.*, OMO shows advantages over them both in transmittance and sheet resistance, as well as being robust and cost-effective.[1] Naturally, OMOs have been widely applied in low temperature processed organic and perovskite solar cells (PSCs).[2–16] In the family of PSCs, OMO exhibits higher and higher potential in high performance device structures.[2,4,5,7,8,10,11,17] In 2015, Yang Yang *et al.* successfully adopted MoOₓ/Au–Ag/MoOₓ as the top transparent conductive electrode of a perovskite top cell in the framework of perovskite/CIGS tandem solar cells, where pre-deposited Au nanodots were used as seed layer to raise compact and smooth silver interlayer of the OMO structures.[11] Employing WO₃/Ag/WO₃ structures as light-in window of inverted planar PSCs, Xue Liu *et al.* developed well-performing flexible devices with PEDOT:PSS as hole-transport layer.[18,19] Although WO₃/Ag/WO₃ shows high transparency owing to the matching of refractive index of each film involved in the OMO structure,[1] PEDOT:PSS is a weakness because of it being extremely sensitive to humidity. In another way, SnO₂/Ag/SnO₂ was successfully used as both top and bottom TCO electrode layer in normal planar PSCs reported by the Riedl group.[5,8] Although SnO₂ can act as good electron transport material in such planar PSCs, SnO₂/Ag/SnO₂ has inferior transmittance in contrast to WO₃/Ag/WO₃ theoretically.[1] In view of the above reports, OMOs have shown promising potential for substituting ITO in solar cells. However, research is still at its initial stage, needing further efforts to optimize the structures and processes in different aspects of the series of materials for their broad and potential applications.

In this work, considering synergistically transmittance, optical matching with glass and electron transport ability as discussed above, WO₃/Ag/SnO₂ (WAS) was selected as a promising OMO candidate to realize high-performance ITO-free PSCs, with an optimal structure combination. Moreover,

19330 | *J. Mater. Chem. A*, 2018, **6**, 19330–19337

This journal is © The Royal Society of Chemistry 2018

interface engineering plays an important role in the evolution of high-performance devices. Soluble 4 nm SnO_2 nanoparticles (NPs) were applied to modify the surface of WAS, and to form a compact and effective electron transport layer. The result is a huge improvement of device performance with conversion efficiency increasing markedly from *ca.* 3% to 14%, which is the highest value reported for PSCs with OMO replacing ITO.

In addition to the factors mentioned above, a closer work function matching contributes to electron transfer at the cathode interface and the balance of both electron and hole transport in the whole device. The optimal enhancement was achieved by tuning the thickness of the SnO_2 NP layer. This effect was explored in detail through various protocols, such as Kelvin probes, ultraviolet photoelectron spectroscopy (UPS), photoluminescence (PL) *etc.* The characterization results prove convincingly the interface band level tuning effect of the SnO_2 NP layer.

Experimental

WAS film fabrication and characterization

Electronic glass (BBL-001, Zhuhai Kaivo Optoelectronic Technol. Co. Ltd) with a thickness of 1 mm was used as a transparent substrate and was washed with acetone, isopropanol and alcohol for 15 min each. The WAS film was prepared by a reactive plasma deposition tool combining electron beam evaporation with a radio frequency ion source (Optical Film Coater, OTFC-900). WO_3, Ag and SnO_2 were sequentially evaporated on the electronic glass substrates. For the evaporation of oxides WO_3 and SnO_2, the substrate was heated to 200 °C and the degree of vacuum was 4×10^{-3} Pa with 20 sccm O_2 and 5 sccm Ar ionized gases. For the evaporation of metal Ag, the substrate was at room temperature and the vacuum degree was 5×10^{-4} Pa without any ionized gas assistance. The transmittance of these WAS films was measured by an ultraviolet-visible absorption spectrometer (PerkinElmer, Lambda 950). The sheet resistances of the films were measured by a four-probe tool. The film adhesive test was carried out by sonication in ethanol solvent.

PSC device fabrication

Unless stated otherwise, all materials were purchased from Sigma-Aldrich or Alfa Aesar and used as received.

The PSC structure was glass/WAS/SnO_2 NPs/$MAPbI_3$/spiro-MeOTAD/MoO_3/Ag. Firstly, the 4 nm SnO_2 colloid precursor (15% (mass fraction) in H_2O colloidal dispersion) was diluted in a ratio of 1 : 5 with deionized water. The SnO_2 NP interlayer was spin-coated on a glass/WAS substrate at 5000 rpm for 30 seconds and then annealed on a hot plate at 180 °C for 30 min. Then, 160 mg MAI and 461 mg PbI_2 were mixed in 75 mL of dimethyl sulfoxide and 640 mL of *N*,*N*-dimethylformamide solution. The solution was heated and stirred at 60 °C in a glove box filled with N_2 for two hours. The perovskite solution was spin-coated (4000 rpm, 30 s) in the N_2 glove box with antisolvent (chlorobenzene) in the first 7 s, and annealed at 75 °C for 15 min and 100 °C for 10 min successively. After that, 45 μL of spiro-

MeOTAD solution, containing 72.3 mg spiro-MeOTAD, 30 μL FK209/acetonitrile (300 mg mL^{-1}), 17.5 μL of lithium bisimide (LiTFSI) solution (520 mg LiTFSI in 1 mL acetonitrile) and 28.8 μL of 4-*tert*-butylpyridine and in 1 mL of chlorobenzene, was spin-coated on the perovskite layer at 4000 rpm for 30 seconds. Finally, a composite cathode electrode layer composed of 10 nm MoO_3 and 100 nm Ag was deposited by thermal evaporation in a background vacuum pressure of 5.0×10^{-4} Pa.

Device characterization

The sheet resistance of the WAS electrodes was obtained by four-probe measurements (RTS-4, 4 Probes Tech.).

The *J–V* curves were obtained *via* a voltaic voltmeter (2400 Apparatus, Keithley). AM1.5G spectrum illumination was provided by 3A solar simulator (Sol 3A, Newport), the light intensity of which was 100 mW cm^{-2} and was calibrated by a standard crystalline silicon solar cell. Reverse scan (1.2 V → −0.2 V, step 0.03 V, delay time 200 ms) and forward scan (−0.2 V → 1.2 V, step 0.03 V, delay time 200 ms) were investigated to demonstrate the electric hysteresis properties. The area of the device was 0.1 cm^2. The external quantum efficiency (EQE) spectra were obtained with an Enli Technology (Taiwan) EQE measurement system (QE-R). The light intensity was calibrated with a standard single-crystal silicon solar cell at each wavelength. Transmission spectra were measured by a UV/Vis/NIR spectrophotometer (Lambda 950, PerkinElmer). Top-view scanning electron microscopy (SEM) images were obtained by a TESCAN MIRA3 scanning electron microscope using an SE2 detector operating at an accelerating voltage of 5 kV. Cross-sectional SEM was conducted *via* a focused ion beam (FEI Helios Nanolab 600i) operating at 30 kV and subsequently imaged with the electron beam of the same instrument using an accelerating voltage of 5 kV. The film surface morphology and surface potentials were investigated by an atomic force microscope (AFM) (MFP-3D-Stand Alone, Asylum Research). Surface work functions of WAS and SnO_2 NP layer were measured by UPS (AXIS Ultra DLD, KRATOS Analytical). A spectrofluorometer (FS5, Edinburgh Instruments) was used for room temperature and time resolved PL spectra and, as excitation source, a 405 nm pulsed laser was used for the time resolved PL measurements. For the light exposure tests, all the unencapsulated devices were illuminated continuously in AM1.5 simulated sunlight in an ambient atmosphere (37% RH and 60 °C).

FDTD solution simulations

Theoretical simulation was conducted *via* finite difference time domain (FDTD) solution software (8.15.736 for x64, Lumerical Inc.). In the 3D FDTD model, the system was made by a 2 nm resolution grid with 2000 fs simulation time. The refractive index *n* and extinction coefficient *k* of Ag and Si were provided by Ag – CRC[20] and Si – Palik,[21] while for the oxides, WO_3 and SnO_2, considering various crystal structures, the *n* and *k* values were measured by a spectroscopic ellipsometer (Uvisel, HORIBA) (Fig. S1 in ESI†). The atmosphere around the structure is set as air whose dielectric constant is one. The boundary of the FDTD region along *Z* axis was set as a perfectly matched

This journal is © The Royal Society of Chemistry 2018

J. Mater. Chem. A, 2018, **6**, 19330–19337 | **19331**

layer whereas the boundaries in X direction and Y direction were both set as periodic. A plane wave source of Bloch/periodic type was chosen at 600 nm wavelength.

Results and discussion

Inspired by the simulation and experimental results in the literature,[22] WO_3/Ag/WO_3 was adopted as a basic structure by us to develop high transparency and high conductivity OMO composed films to replace ITO. However, the direct contact between WO_3 and perovskite easily leads to degradation of perovskite films and the initial device performance is also poor, as recorded in our earlier experiments. Thereafter, SnO_2 popular in PSCs was selected as the intimate film to contact the perovskite absorber layer in the PSC device structure. Fig. 1a and b show the silver thickness dependent transmittance and sheet resistance variations in a default WO_3 (30 nm)/Ag (x nm)/SnO_2 (30 nm) structure referring to the optimized parameters in the literature.[22] The film thickness was measured each time directly by the monitor equipped in the process system and calibrated at the initial stage by the step profiler with each kind of film on quartz substrates. A 10.7 nm thick silver film sandwiched in the WAS structure shows both optimal transmittance over the spectrum from 400 nm to 850 nm, which is the main absorption range of the perovskite absorber layer, and low sheet resistance, which is obviously lower than that of commercial ITO films. To further define the best combination of the other two film thicknesses in the WAS structure, a film thickness

modulation was carried out with fixing the thickness of the silver layer at 10.7 nm. The simulated and experimental contour plots of transmittance ($\lambda = 600$ nm) for WO_3 (x nm)/Ag (10.7 nm)/SnO_2 (y nm) as a function of x and y are shown in Fig. 1c and d, respectively. Both the simulation and experimental results show the same trend when tuning the thicknesses of WO_3 and SnO_2, except for mismatches in some local distributions. In most cases, the calculation suffers to a large extent from its mismatch with the experimental results. Different from former reports,[9,22,23] we carried out intensive experiments to collect a large number of data points collected in Fig. 1d, to obtain the realistic best region for design of OMO structures. As shown in Fig. 1c and d, the transmittance is more sensitive to the variation of SnO_2 thickness than to that of WO_3. Extracted from the data of Fig. 1d, S2a and b† presents the transmission property over the whole spectrum (from 400 nm to 850 nm) depending only on one dimensional variation of the thickness of WO_3 or SnO_2, which clearly shows the thickness tuning effect of them on the transmission spectra of full wavelength. The green block line in Fig. S2a† shows comparably superior transmission property over other combinations while the red block line in Fig. S2b† turns out to be the best one. As the dashed lines in Fig. 1c and d show, the optimized WAS structure in our work was finalized at $x = 23$ nm and $y = 35$ nm, which are within a considerably broad process window.

To clarify the transmittance difference and function of each component film in the WAS, the transmittance spectra of all films and combinations involved as well as ITO film used in this
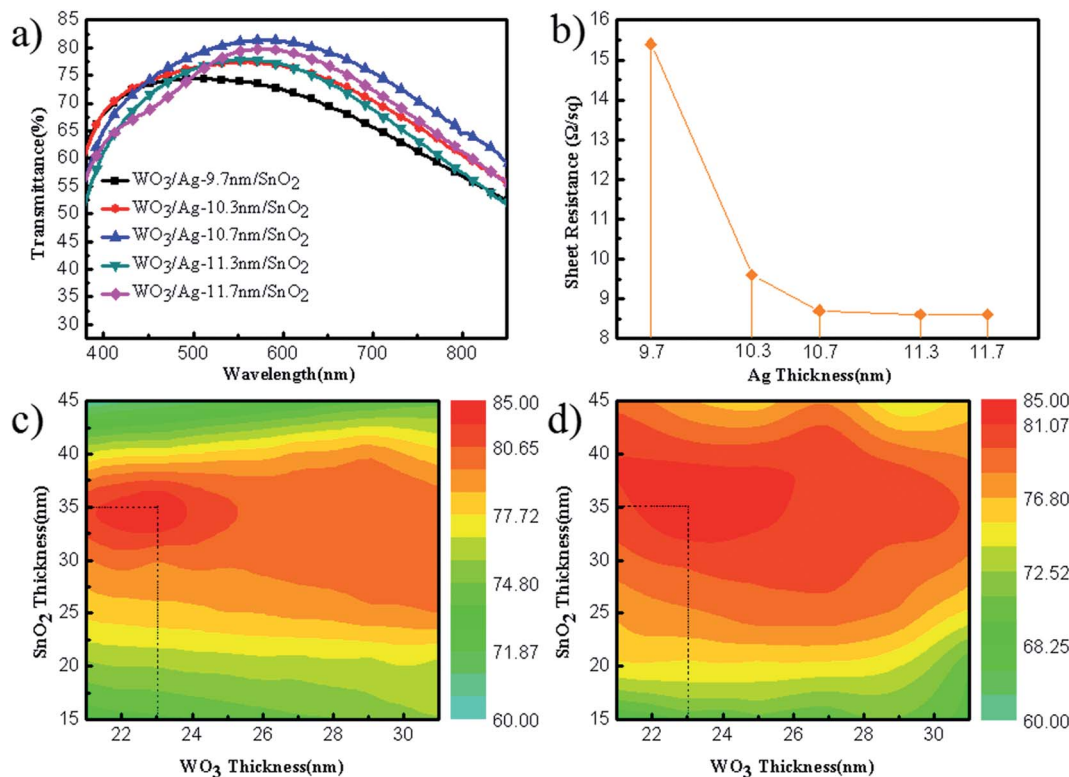

Fig. 1   (a) Transmission spectra and (b) sheet resistances with different silver interlayer thickness in a default OMO structure of WO_3 (30 nm)/Ag/SnO_2 (30 nm). (c) Simulated and (d) experimental contour plots of the transmission spectra of WO_3 (x nm)/Ag (10.7 nm)/SnO_2 (y nm) structure (the Ag layer is fixed at 10.7 nm).
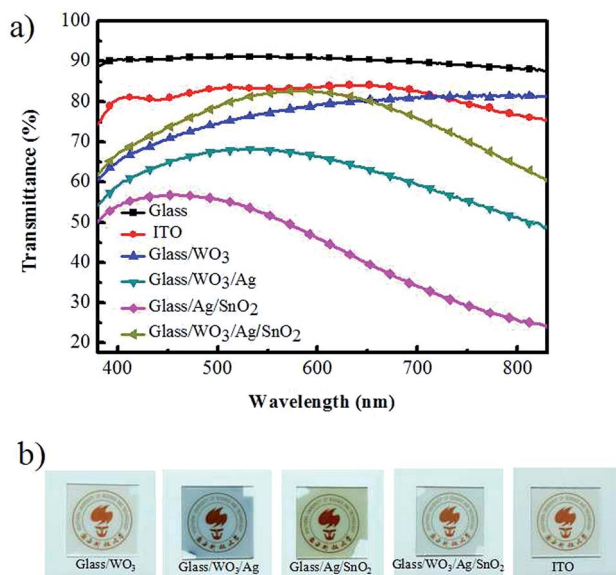
Fig. 2 (a) Transmission spectra and (b) optical images of different film combinations of the WAS structure compared with commercial ITO substrates.

work are plotted in Fig. 2a. Owing to matching of the refractive indexes among each component of glass/WO_3/Ag/SnO_2, the WAS structure shows considerably high transmittance ranging from 400 nm to 850 nm, although it still stays lower in some part of the solar spectrum than that of commercial ITO films. Fig. 2b shows optical images of each combination film deposited on the blank glass along with ITO. The transmittance differences can also be discriminated. The transmittance goes from high to low as the combination changes from glass/WO_3 to either glass/WO_3/Ag or glass/Ag/SnO_2. After depositing SnO_2 on the as-prepared glass/WO_3/Ag substrates, the transmittance becomes higher again and becomes comparable to that of the commercial ITO substrates.

Post thermal annealing at suitable temperature can assist recrystallization and reorganization of as-deposited polycrystalline

or amorphous films composed of NPs, thereby enhancing the crystallinity and compactness of the films, increasing the dielectric constant of dielectric films and finally improving the transmittance.[23,24] Fig. 3 shows the sheet resistance and transmittance of the WO_3 (23 nm)/Ag (10.7 nm)/SnO_2 (35 nm) structure as a function of thermal annealing temperature. The sheet resistance decreases slowly as the annealing temperature increases and the lowest point is reached at 350 °C as the red line shows in Fig. 3a. After that, it rises sharply, which announces an obvious change of OMO structure. Meanwhile, the transmittance breaks down when the annealing temperature reaches 450 °C while it has little variation from room temperature to 400 °C. So the optimal post thermal annealing temperature was set at 350 °C in our work. According to the variation of sheet resistance described above, the thermal annealing can contribute to flatten the as-deposited metal islands and increase connection between each island, and hence weaken localized surface plasmonic coupling and increase the transmittance as well as conductivity.[23–25] Ultrahigh annealing temperature would destroy the metastable structure of the WAS composite films and damage both transmittance and conductivity. In addition to conductivity and transmittance, the WAS film robustness can also be realized by thermal annealing, which is also an important criterion for its application. Before post annealing, the as-prepared WAS film is easily exfoliated by sonication in the following solar cell fabrication process while it keeps stable in sonication for over 90 minutes after 350 °C thermal annealing (blue line in Fig. 3a).

Depending on the optimized WAS transparent conductive film, a planar device in a configuration of "glass/WAS/$MAPbI_3$/spiro-MeoTAD/MoO_3/Ag" was fabricated to replace conventional ITO glass. It should be noted here that $MAPbI_3$ just acts as a mature absorber perovskite layer to evaluate the performance of the WAS composite film with which we are concerned in this work. Without any modification of the pristine WAS surface, the device performance is really poor with small current density (J_{sc}) and fill factor (FF) while the open circuit voltage (V_{oc}) stays around 1.0 V and seems reasonable (Fig. S3a†). The reasonable V_{oc} value indicates the photon-generated electrons and holes are effectively separated and reach their respective electrodes.
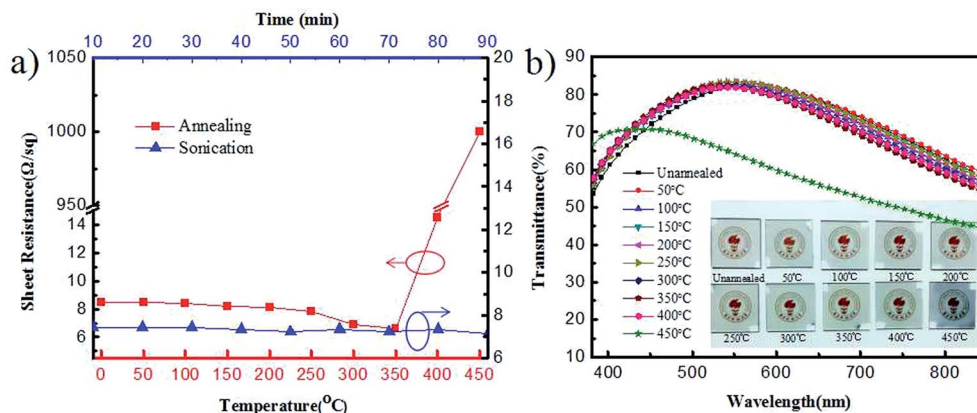

Fig. 3 (a) Sheet resistance (red line) of the WAS film annealed at different temperatures for one hour in air; and the variation of sheet resistance (blue line) of the WAS film annealed at 350 °C with sonication for different times. (b) Transmission spectra of the WAS films annealed at different temperatures for one hour in air.

That is different from the behavior in the device with a configuration of "glass/ITO/MAPbI$_3$/spiro-MeoTAD/MoO$_3$/Ag", where electrons and holes can reach the ITO electrode simultaneously and hence leading to lower V_{oc} (Fig. S3b†).[26] However, low J_{sc} and FF of the WAS-based device can be attributed to low charge transfer rate, especially electron transfer rate at the cathode side, because of its lack of electron transport layer.[27–30] The result demonstrates the synthesized SnO$_2$ layer in the WAS is not strong enough for electron transfer in the device. Driven by this interface engineering requirement, soluble SnO$_2$ NPs of 4 nm in mean size were applied to enhance electron transfer in the WAS-based devices.

Fig. 4a shows a typical cross-sectional SEM image of the WAS device, which was prepared by a focus ion beam tool with Ga ions. The MAPbI$_3$ perovskite layer is about 370 nm thick with well-crystalline grains wrapping through the absorber layer. The top-view image of the perovskite film coated on the WAS

substrate is shown in the insert, examining the grain sizes and good crystallinity of the film involved. The thickness of spiro-MeoTAD layer is about 200 nm, with MoO$_3$ (10 nm)/Ag (100 nm) on the top, which are consistent with some former reports. What attracts us is the WAS film with a total thickness of about 60 nm. SnO$_2$ NPs modification layer is ambiguous in the device structure and has a thickness of *ca.* 10 nm, which is investigated individually on the bare glass by AFM. It is also difficult to discriminate the interface between SnO$_2$ and WO$_3$ in the WAS composite film, which may result from the post thermal annealing. However, the bright spots in the WAS region indicate the existence of silver NPs film inside. Through AFM topographic images shown in Fig. S4,† the surface roughness became larger after spin coating of this SnO$_2$ NPs solution, rising from *ca.* 1 nm to 2.5 nm on average. The device structure is schematically illustrated in Fig. 4b.
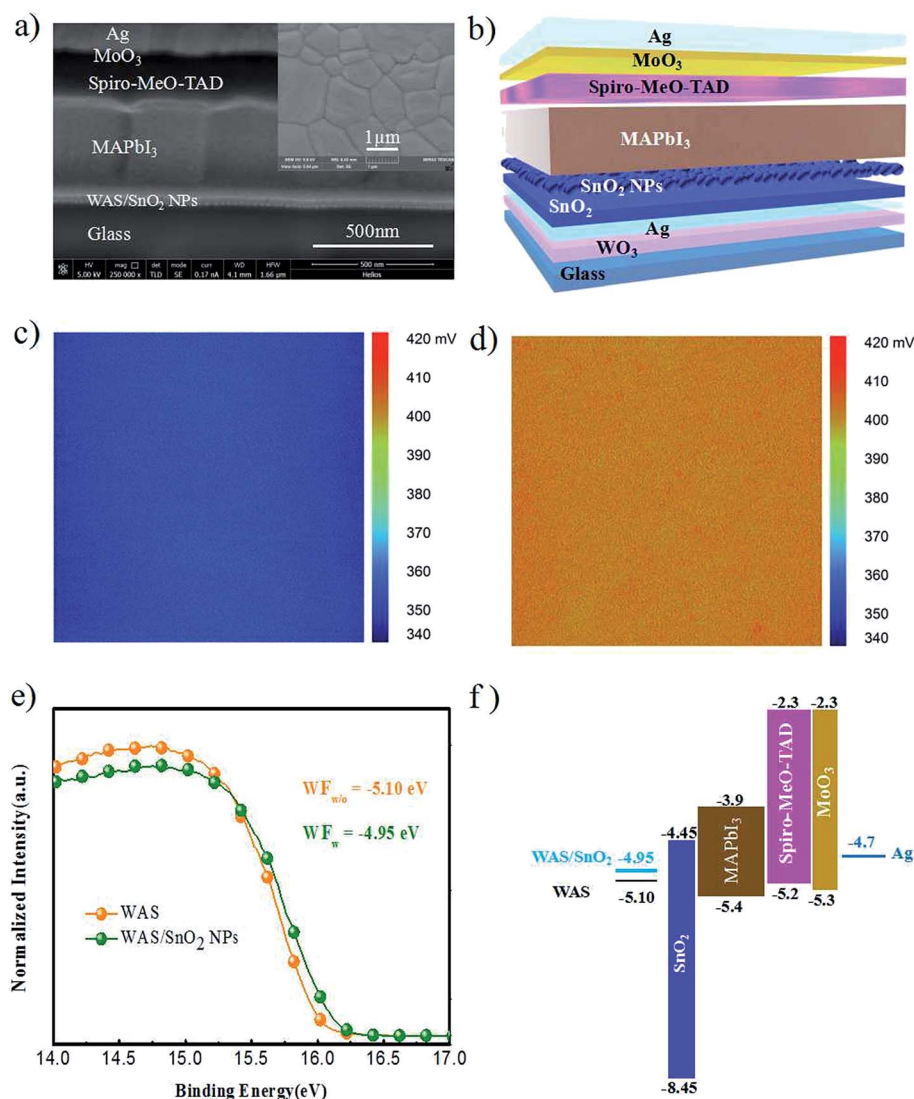

Fig. 4 (a) Cross-sectional SEM image of the PSC based on the WAS substrate with modification of SnO$_2$ NPs. The inset is a top-view SEM image of MAPbI$_3$ film deposited on the SnO$_2$ NP-coated WAS substrate. (b) Schematic configuration of a typical device. Scanning Kelvin Probe Microscopy (SKPM) images of (c) the bare WAS and (d) the SnO$_2$ NP-modified WAS films on glass. The scan size is 5 μm × 5 μm. (e) UPS spectra of the bare WAS (yellow line) and the SnO$_2$ NP-modified WAS films (green line) on glass. (f) Energy level diagram of each material in the device.

To reveal the function of SnO_2 NPs, Kelvin probes and UPS were applied to investigate the work function variation before and after modification by a layer of SnO_2 NPs. The surface potential is augmented after this modification, increasing from 350 mV to 405 mV (Fig. 4c and d). The positive increase of the surface potential indicates the work function of the WAS film is increased by this modification, better matching the conduction band minimum (CBM) of the perovskite layer and facilitating electron transfer at the interface.[31,32] According to the relationship between the work function (φ_{sample}) and the surface potential (V_{sp}) of samples, $\varphi_{sample} = \varphi_t + eV_{sp}$, where φ_t is the work function of conductive tip, the work function of the pristine WAS and the SnO_2 NP-modified WAS films can be determined as -5.02 eV and -4.97 eV, respectively. This decrease in the work function was further confirmed by the UPS data (Fig. 4e), which show a decrease from -5.10 eV to -4.95 eV. This SnO_2 NPs layer accounts for at least two functions besides the modulation of work function of the WAS electrode. On the one hand, depending on its suitable CBM and valence band maximum compared with $MAPbI_3$, this SnO_2 NPs interlayer enhances the ability of both transporting electrons and blocking holes. This is because SnO_2 NPs colloidal solution easily forms a dense and pinhole-free SnO_2 film, which is crucial for device performance.[28] On the other hand, SnO_2 NPs colloidal precursor-derived films have remarkable advantages over those obtained using other synthesis methods in device performance, which may be attributed to different oxygen vacancy concentration in the lattice of SnO_2 NPs films synthesized by different methods.[33] Fig. 4f summarizes the above results into an electronic structure of the whole device for clear understanding of charge transfer inside the system.

Because of the function of the layer of SnO_2 NPs, the device conversion efficiency was boosted to 14% (Fig. 5a), which is the highest value reported so far for OMO-based PSCs.[2,5,8,10,11,17] For the device parameters of the optimum cell, the J_{sc} doubles from 7.9 mA cm^{-2} to 18.6 mA cm^{-2} and FF triples from 0.24 to 0.72, in contrast to the WAS-based device without modification of the SnO_2 NPs layer. The V_{oc} also increases from 0.98 V to 1.045 V. The current density is also confirmed by integrating the EQE spectrum (Fig. 5b) of the device. The hysteresis loop is also suppressed by modulating electron transfer and hence balancing the total charge transport at each end of the whole device.[34,35] For the as-purchased 4 nm SnO_2 NPs aqueous solution, the original concentration was 15% in terms of mass fraction, which was diluted to different concentrations with deionized water. Fig. S5† collects the J–V curves of devices depending on different concentration of the SnO_2 NPs solution. Among them, the device based on a concentration of 2.5% (mass fraction) shows the highest performance. Higher or lower concentration may result in a thick or uncovered modification layer, both of which would affect the electron transfer at the interface. The statistical data of each device parameter in a batch of 24 PSCs are summarized in Fig. 5c and d and their distributions are also collected in Table S1.†

The electron extraction power of the SnO_2 NPs layer was further characterized by PL and time resolved PL (Fig. 6). The quenching effect of the SnO_2 NPs layer is larger compared with the bare WAS film (Fig. 6a). The time resolved PL spectra further
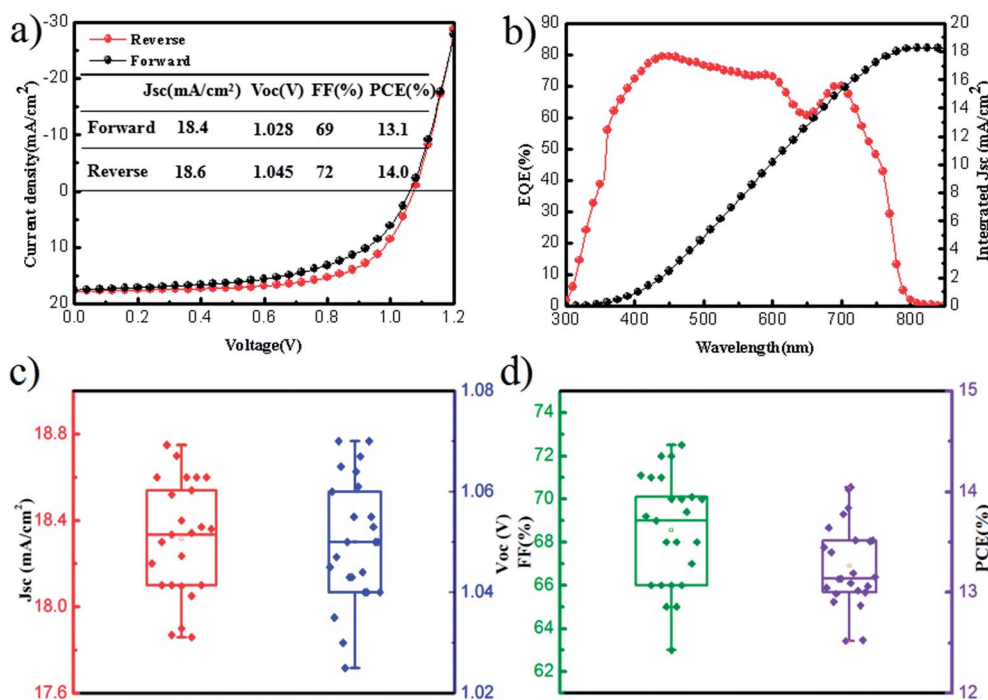

Fig. 5 (a) Forward and reverse J–V characteristics of the optimum cell with SnO_2 NP-modified WAS as transparent conductive electrodes under illumination of AM1.5G solar simulator (100 mW cm^{-2}). (b) EQE spectra and integrated current density of the device in (a). Statistics of J_{sc} (red) and V_{oc} (blue) in (c), and FF (green) and PCE (purple) in (d) for a batch of 24 devices.
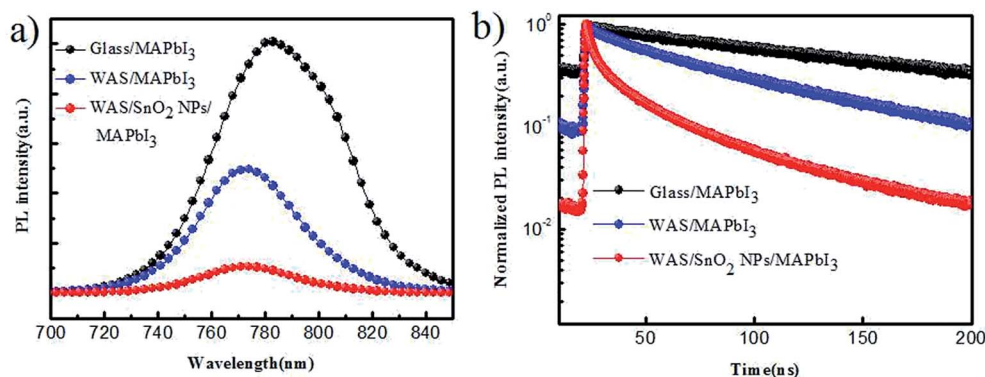
Fig. 6 (a) Steady state PL and (b) time resolved PL spectra for perovskite films on different substrates.

confirm the charge transfer rate sequence among the three kinds of samples, which can be fitted to a biexponential decay: $I(t) = A_1 \exp(t/\tau_1) + A_2 \exp(t/\tau_2)$. It can be used to identify the two stage decay time and the average lifetime can then be determined as $\tau_{avg} = \left(\sum_i A_i \tau_i^2 \right) \Big/ \left(\sum_i A_i \tau_i \right)$.[36] The calculated data are summarized in Table S2.† The result further confirms the electron extraction ability of the SnO$_2$ NPs layer, which contributes directly to the enhancement of the device performance.

In order to compare the stability between the WAS-based structure and commercial ITO, the device stability was also investigated *via* continuous light exposure under one standard sunlight (1000 W m^{-2}). It should be noted that the devices are unencapsulated and tested in the same environment (37% RH, 60 °C). Both kinds of devices have the same device structure except for the difference of the transparent conductive layer. The results in Fig. S6† show two degradation stages for both devices. Before 500 minutes, the degradation rate for them is similar and mixed. After that, the rate is different. The WAS-based device exhibits faster degradation than the ITO-based one. However, the rate difference is small and only 10–20% in conversion efficiency remained after light exposure for 1000 minutes. According to former reports, the cross diffusion of silver atoms and halide ions may contribute mainly to this degradation.[37–40] Hence the greater degradation rate of the WAS-based device may be attributed to the extra silver layer in the composed film structure. However, the comparison result demonstrates the stability of our WAS films is promising, while more efforts are needed to optimize the OMO structure and further to improve its stability.

Conclusion

Through optic simulations and intensive attempts to modulate film thickness combination of the OMO structure, WO$_3$ (23 nm)/Ag (10.7 nm)/SnO$_2$ (35 nm) with maximum transmittance and lowest sheet resistance was successfully prepared by reactive plasma deposition. Post thermal annealing is necessary and accounts for the enhancement of mechanical stability and film crystallinity. The bare WAS composite film cannot act as both

good TCO and suitable electron transport layer simultaneously. The well-known 4 nm SnO$_2$ NPs solution was applied to tune the work function of WAS from -5.10 to -4.95 eV and also to enhance the electron transfer and selectivity. Owing to the SnO$_2$ NPs interface layer, the device conversion efficiency was boosted to 14% with J_{sc} doubling from 7.9 mA cm^{-2} to 18.6 mA cm^{-2} and FF tripling from 0.24 to 0.72. This conversion efficiency is the highest value reported so far, reaching the edge of the reasonable region of ITO- and MAPbI$_3$-based device performances. In the continuous light exposure durability test, the WAS-based devices also show comparable stability with the ITO-based ones. However, research still stays at its initial stage and more efforts are needed from all aspects to develop OMO-based solar cells and other optoelectronic devices.

Contributions

Both Dr F. X. Liang and Y. Lin mainly completed the optimization of the WAS structures and the perovskite solar cells, and took part in writing the paper. Z. F. He and T. Chen contributed to the optimization of the WAS structure. W. Chen conducted the processing of perovskite solar cells. Y. D. Zhu conducted the simulation along with S. M. Ma. Y. H. Wu conducted the AFM and Kelvin probes testing. B. Tu joined the device performance optimization. L. Liang, Dr Z. X. Zhang and Dr D. Wang gave constructive suggestions in the optimization and mechanism discussion. Prof. L. B. Luo revised and improved the quality of the manuscript. Prof. Z. B. He conceived the idea, directed the process and wrote the manuscript.

Conflicts of interest

There are no conflicts to declare.

Acknowledgements

References

1 S. Kim and J. L. Lee, *J. Photonics Energy*, 2012, **2**, 021215–021237.

2 E. Lee, J. Ahn, H.-C. Kwon, S. Ma, K. Kim, S. Yun and J. Moon, *Adv. Energy Mater.*, 2018, **8**, 1702182.

3 Y. X. Ji, J. Yang, W. Luo, L. L. Tang, X. X. Bai, C. Q. Leng, C. Y. Ma, X. Z. Wei, J. Wang, J. Shen, S. R. Lu, K. Sun and H. F. Shi, *ACS Appl. Mater. Interfaces*, 2018, **10**, 9571–9578.

4 G. K. Dalapati, A. K. Kushwaha, M. Sharma, V. Suresh, S. Shannigrahi, S. Zhuk and S. Masudy-Panah, *Prog. Mater. Sci.*, 2018, **95**, 42–131.

5 J. Zhao, K. O. Brinkmann, T. Hu, N. Pourdavoud, T. Becker, T. Gahlmann, R. Heiderhoff, A. Polywka, P. Görrn, Y. Chen, B. Cheng and T. Riedl, *Adv. Energy Mater.*, 2017, 7, 1602599.

6 Y. Zhang, Y. X. Cui, T. Ji, Y. Y. Hao and F. R. Zhu, *IEEE Photonics J.*, 2017, **9**, 1–7.

7 K. T. Lee, J. Y. Jang, S. J. Park, S. A. Ok and H. J. Park, *Nanoscale*, 2017, **9**, 13983–13989.

8 T. Hu, T. Becker, N. Pourdavoud, J. Zhao, K. O. Brinkmann, R. Heiderhoff, T. Gahlmann, Z. Huang, S. Olthof, K. Meerholz, D. Tobbens, B. Cheng, Y. Chen and T. Riedl, *Adv. Mater.*, 2017, **29**, 1606656–1606665.

9 I. S. Oh, C. H. Ji and S. Y. Oh, *Electron. Mater. Lett.*, 2016, **12**, 156–162.

10 X. Liu, X. Y. Guo, Z. H. Gan, N. Zhang and X. Y. Liu, *J. Phys. Chem. C*, 2016, **120**, 26703–26709.

11 Y. M. Yang, Q. Chen, Y. T. Hsieh, T. B. Song, N. D. Marco, H. Zhou and Y. Yang, *ACS Nano*, 2015, **9**, 7714–7721.

12 H. Kim, K. T. Lee, C. M. Zhao, L. J. Guo and J. Kanicki, *Org. Electron.*, 2015, **20**, 103–111.

13 J. Zou, C. Z. Li, C. Y. Chang, H. L. Yip and A. K. Jen, *Adv. Mater.*, 2014, **26**, 3618–3623.

14 Z. Xue, X. Liu, N. Zhang, H. Chen, X. Zheng, H. Wang and X. Guo, *ACS Appl. Mater. Interfaces*, 2014, **6**, 16403–16408.

15 S. Vedraine, A. El Hajj, P. Torchio and B. Lucas, *Org. Electron.*, 2013, **14**, 1122–1129.

16 S. Schubert, J. Meiss, L. Muller-Meskamp and K. Leo, *Adv. Energy Mater.*, 2013, **3**, 438–443.

17 X. Liu, X. Y. Guo, Y. Lv, Y. S. Hu, J. Lin, Y. Fan, N. Zhang and X. Y. Liu, *ACS Appl. Mater. Interfaces*, 2018, **10**, 18141–18148.

18 W. Chen, K. Li, Y. Wang, X. Feng, Z. Liao, Q. Su, X. Lin and Z. He, *J. Phys. Chem. Lett.*, 2017, **8**, 591–598.

19 Y. Wu, Z. Wang, X. Liu, X. Shen, Q. Zheng, Q. Xue and J. K. Kim, *ACS Appl. Mater. Interfaces*, 2017, **9**, 9059–9069.

20 W. M. Haynes, *CRC handbook of chemistry and physics*, CRC Press, 2014.

21 E. D. Palik, *Handbook of optical properties of solids*, Academic, Orlando, 1985.

22 K. Hong, K. Kim, S. Kim, I. Lee, H. Cho, S. Yoo, H. W. Choi, N. Y. Lee, Y. H. Tak and J. L. Lee, *J. Phys. Chem. C*, 2011, **115**, 3453–3459.

23 A. Dan, H. C. Barshilia, K. Chattopadhyay and B. Basu, *Renewable Sustainable Energy Rev.*, 2017, **79**, 1050–1077.

24 B. Lin, C. Lan, C. Li and Z. Chen, *Thin Solid Films*, 2014, **571**, 134–138.

25 X. Guo, X. Liu, F. Lin, H. Li, Y. Fan and N. Zhang, *Sci. Rep.*, 2015, **5**, 10569.

26 G. J. Meyer, *ACS Appl. Energy Mater.*, 2018, **1**, 1–2.

27 D. Liu, J. Yang and T. L. Kelly, *J. Am. Chem. Soc.*, 2014, **136**, 17116–17122.

28 W. Ke, G. Fang, Q. Liu, L. Xiong, P. Qin, H. Tao, J. Wang, H. Lei, B. Li, J. Wan, G. Yang and Y. Yan, *J. Am. Chem. Soc.*, 2015, **137**, 6730–6733.

29 X. Xu, Q. Chen, Z. Hong, H. Zhou, Z. Liu, W. H. Chang, P. Sun, H. Chen, N. De Marco, M. Wang and Y. Yang, *Nano Lett.*, 2015, **15**, 6514–6520.

30 P. Cui, D. Wei, J. Ji, D. Song, Y. Li, X. Liu, J. Huang, T. Wang, J. You and M. Li, *Sol. RRL*, 2017, **1**, 1600027.

31 W. Chen, L. Xu, X. Feng, J. Jie and Z. He, *Adv. Mater.*, 2017, **29**, 1603923.

32 C. Xiao, C. Wang, W. Ke, B. P. Gorman, J. Ye, C. S. Jiang, Y. Yan and M. M. Al-Jassim, *ACS Appl. Mater. Interfaces*, 2017, **9**, 38373–38380.

33 Q. Jiang, X. Zhang and J. You, *Small*, 2018, **14**, 1801154.

34 X. Meng, J. Zhou, J. Hou, X. Tao, S. H. Cheung, S. K. So and S. Yang, *Adv. Mater.*, 2018, **30**, e1706975.

35 X. Bao, J. Wang, Y. Li, D. Zhu, Y. Wu, P. Guo, X. Wang, Y. Zhang, J. Wang, H.-L. Yip and R. Yang, *Adv. Mater. Interfaces*, 2017, **4**, 1600948.

36 X. Feng, H. Su, Y. Wu, H. Wu, J. Xie, X. Liu, J. Fan, J. Dai and Z. He, *J. Mater. Chem. A*, 2017, **5**, 12048–12053.

37 Y. Kato, L. K. Ono, M. V. Lee, S. Wang, S. R. Raga and Y. Qi, *Adv. Mater. Interfaces*, 2015, **2**, 1500195.

38 W. Chen, G.-n. Zhang, L.-m. Xu, R. Gu, Z.-h. Xu, H.-j. Wang and Z.-b. He, *Materials Today Energy*, 2016, **1–2**, 1–10.

39 E. M. Sanehira, B. J. Tremolet de Villers, P. Schulz, M. O. Reese, S. Ferrere, K. Zhu, L. Y. Lin, J. J. Berry and J. M. Luther, *ACS Energy Lett.*, 2016, **1**, 38–45.

40 Z. Li, C. Xiao, Y. Yang, S. P. Harvey, D. H. Kim, J. A. Christians, M. Yang, P. Schulz, S. U. Nanayakkara, C.-S. Jiang, J. M. Luther, J. J. Berry, M. C. Beard, M. M. Al-Jassim and K. Zhu, *Energy Environ. Sci.*, 2017, **10**, 1234–1242.

This journal is © The Royal Society of Chemistry 2018

J. Mater. Chem. A, 2018, **6**, 19330–19337 | **19337**